Stress fields of finite-size dislocation walls and prediction of back stress induced by geometrically necessary dislocations at grain boundaries

Maoyuan Jiang, Ghiath Monnet, Benoit Devincre

To cite this version:

Maoyuan Jiang, Ghiath Monnet, Benoit Devincre. Stress fields of finite-size dislocation walls and prediction of back stress induced by geometrically necessary dislocations at grain boundaries. Journal of the Mechanics and Physics of Solids, 2020, 143, pp.104071. 10.1016/j.jmps.2020.104071 . hal-02887595

HAL Id: hal-02887595
https://cnrs.hal.science/hal-02887595

Submitted on 30 Jul 2020

Stress fields of finite-size dislocation walls and prediction of back stress induced by geometrically necessary dislocations at grain boundaries

Maoyuan Jiang[a,b], Ghiath Monnet[a], Benoit Devincre[b,*]

[a] *EDF R&D, MMC, Avenue des Renardières, 77818, Moret-sur-Loing, France*
[b] *CNRS - ONERA, LEM, 29 Avenue de la Division Leclerc, 92322 Chatillon, France*

Abstract

At low strain, geometrically necessary dislocations (GND) confined in the close vicinity of grain boundaries can be approximated as a dislocation wall structure called a GND facet. Analytical solutions derived from Field Dislocations Mechanics (FDM) theory allow calculating the stress components associated with the GND facets but are unable to account for the stress field variation induced by finite size effect. Dislocation dynamics simulation is used to investigate the true stress field of GND facets. The geometry, dimension and dislocation density of three generic types of GND facets (twist, tilt and epitaxial facets) are systematically studied. In all cases, the stress field generated by GND facets is proportional to the surface GND density and its spatial distribution can be recovered using FDM solution combined with two scaling parameters identified from DD simulation results. This calculation procedure can be generalized to any crystal structure by relating the components of the surface Nye's tensor to the solutions of simple cubic slip systems. Finally, static and dynamic tests are made to validate the calculation of back stress within regular grains bounded by GND facets.

Keywords: Grain boundaries, Polycrystal, Geometrically necessary dislocations, Crystal plasticity, Dislocation Dynamics

---

1. Introduction

Grain boundaries (GB) in polycrystals are surface defects accommodating the crystalline disorientation between grains. The atoms at GBs are repositioned and arranged into facets that minimize the crystal elastic energy at room temperature (Hsieh and Balluffi, 1989, Sutton and Balluffi, 1995). Influence of GBs on the polycrystal properties are numerous, but its major effect is associated with the process of plastic strain hardening. During plastic deformation, GBs impede the motion of dislocations and reduce the dislocation mean free path, then a larger applied stress is required to produce plastic deformation. In other words, dislocations accumulate at GBs and generate increasing internal stresses with the plastic deformation, i.e., strain hardening (Jiang et al., 2019). GBs with a misorientation angle larger than 15 degrees are dominant in polycrystals and act as strong barriers to dislocation dynamics. Configurational energy makes such defects very stable and the transmission of dislocations from one grain to the next implies large stresses (Kondo et al., 2016). Hence, the propagation of plastic slip across adjacent grains is possible at low strain only by the indirect transmission of dislocations in some particular GB facets (Priester, 2013) or with the activation of dislocation sources (Lee et al., 1990, Malyar et al., 2017). A large number of dislocations are then accumulated at or very close to the GBs during the first stages of plastic deformation (Amouyal et al., 2005, Shih and Li, 1975).

Dislocations accumulation at GBs has been reported many times for metals and alloys under monotonic and cyclic loading (Feaugas, 1999, Mughrabi, 1988). The dislocation microstructure observed at GBs is increasingly heterogeneous when decreasing the grain size or increasing plastic deformation (Caballero et al., 2011, He et al., 2018). Unlike the forest or statistically stored dislocations (SSD) density measured inside the grain, the dislocation density accumulated at GBs is polarized, i.e. the total Burgers vector is non-zero. Hence, the dislocation network observed at GBs is made of geometrically necessary dislocations (GND) (Ashby, 1970), which accommodates the strain incompatibility imposed by a non-uniform plastic deformation inside grains (Arsenlis and Parks, 1999a, Gao and Huang, 2003). Then long-range stresses develop inside the grains as a result of GND density accumulation at the GBs. This stress is commonly defined as a "back stress" opposed to the external loading (Cheng et al., 2018, Fleck et al., 2003, Wu et al., 2015). Many attempts have been made to compute such back stress using, for instance, strain gradient plasticity theory (Aifantis, 1999, Fleck et al., 1994, Gao et al., 1999). Those attempts were recently summarized in (Liu and Dunstan, 2017). The main outcome of this analysis is that all existing quantitative theories involve at least one length scale parameter to be adjusted from experimental data.

Understanding the arrangement details of GND in crystals is essential to develop a back stress model. This is why various experimental techniques, including EBSD (Calcagnotto et al., 2010, Jiang et al., 2013), TEM (Dubinko et al., 2017, Peeters et al., 2001) and X-Ray Diffraction (Ohashi et al., 2009, Yang et al., 2011), have been used to identify the GND distributions.

---

[*] Corresponding author : devincre@onera.fr

Most techniques indicate the existence of a large GND density close to GBs even after a small plastic deformation. On the modeling side, such feature was reproduced by crystal plasticity calculations of polycrystalline aggregates (Berbenni et al., 2020, Cordero et al., 2012, Haouala et al., 2020, Sun et al., 2019). In a recent investigation based on Dislocation Dynamics (DD) simulations (Jiang et al., 2019), it was also shown that the dislocation storage rate $\mathrm{d}\rho/\mathrm{d}\gamma$ recorded inside grains agrees with a prediction of Ashby (Ashby, 1970), i.e., is proportional to the inverse of grain size $1/d$. In addition, DD simulations, in good agreement with experimental observations, show that the dislocation distribution inside the grains is made of SSD density in the bulk and a much larger GND density close to GBs. This distribution of the dislocation density motivates possible calculations of the back stress inside grains considering only the GND density at GBs.

In the literature, many works investigated the long-range stress field associated with dislocation walls or subgrain boundaries using the elastic theory (Gibeling and Nix, 1980, Li and Needham, 1960, Lubarda and Kouris, 1996, Saada and Bouchaud, 1993). Those works allowed modeling the stress fields associated with dislocation cell structures (Mughrabi, 1983), geometrically necessary boundaries (Khan et al., 2004) or dislocation network at precipitate interfaces (Huang et al., 2018). In this paper, a new approach making use of the Field Dislocation Mechanics (FDM) theory (Acharya, 2001) is proposed. This empirical approach allows calculating the stress field associated with GND density organized in facets. Such facets are equivalent to wall structures of finite size (in height and length) containing discrete regularly spaced dislocations. The calculation we proposed is general and allows evaluating with semi-empirical equations the internal stress inside grains with faceted shapes once the dislocation density deposited at the GBs is known.

The paper is organized as follows. In §2, FDM theoretical solutions to calculate stress fields for infinite dislocation walls are briefly presented. In §3, a set of equations are developed to predict the stress field associated with any type of GND facet. In §4, a comparison is made between the proposed analytical model and the results of DD simulations in the case of model configurations. Finally, §5, is devoted to concluding remarks.

2. FDM theoretical solutions for infinite dislocation walls

In this section, analytical expressions for the stress field associated with finite polarized dislocation walls or GND density facets are presented. Such expressions are based on the results of FDM theory and are validated by comparison with discrete dislocation solutions.

The FDM theory is rooted from the pioneering crystal plasticity model first developed by Acharya (Acharya, 2001) and later extended in (Acharya, 2002, 2004). The FDM theory can be applied to problems including the mechanical response associated with a single, a few or a distribution of dislocations in isotropic/anisotropic and linear/nonlinear elastic solids. Examples of FDM calculations solved with FEM simulations are reported for divers configurations in (Roy and Acharya, 2005). While the full theory includes solutions for the transport and evolution of dislocation density, here we limit the FDM approach to the calculation of stress and displacement fields of surface dislocation density.

The FDM elasto-static field equations used in the present study are derived from the elastic displacement field $\underline{\boldsymbol{u}}_e$ for any dislocation density field constrained with conventional boundary conditions. In a small strain setting, a dislocation density inside the body B (with boundary ∂B) is assumed to be immobile and the whole system is in equilibrium. Then, assuming homogeneous linear isotropic elasticity, the following equations must be satisfied :

$$\begin{aligned} &curl\ \underset{\sim}{\boldsymbol{U}}_e = \underset{\sim}{\boldsymbol{\alpha}} \\ &\underset{\sim}{\boldsymbol{\sigma}} = \underset{\approx}{\boldsymbol{C}} : \underset{\sim}{\boldsymbol{U}}_e^{sym} = \underset{\approx}{\boldsymbol{C}} : \underset{\sim}{\boldsymbol{\varepsilon}}_e \\ &div\ \underset{\sim}{\boldsymbol{\sigma}} = 0 \end{aligned} \tag{1}$$

where $\underset{\sim}{\boldsymbol{\alpha}}$ is the excess dislocation density tensor form usually denoted as the Nye's tensor (Nye, 1953), $\underset{\sim}{\boldsymbol{\sigma}}$ is the symmetric Cauchy stress tensor, $\underset{\sim}{\boldsymbol{U}}_e^{sym} = \underset{\sim}{\boldsymbol{\varepsilon}}_e$ is the elastic strain tensor and $\underset{\approx}{\boldsymbol{C}}$ is the fourth-order elastic moduli tensor. Boundary conditions are defined in a standard manner. A prescribed traction vector field $\underline{\boldsymbol{t}}_d$ is applied to a part ∂B_t of the boundary ∂B, and the other part ∂B_u is subjected to the prescribed displacement $\underline{\boldsymbol{u}}_d$ such that :

$$\begin{aligned} &\underset{\sim}{\boldsymbol{\sigma}} \cdot \underline{\boldsymbol{n}} = \underline{\boldsymbol{t}}_d \quad \text{on } \partial B_t \\ &\underline{\boldsymbol{u}}_e = \underline{\boldsymbol{u}}_d \quad \text{on } \partial B_u \end{aligned} \tag{2}$$

The elastic distortion tensor of a continuum body elasto-plastically deformed is written as the sum of two parts :

$$\underset{\sim}{\boldsymbol{U}}_e = \underset{\sim}{\boldsymbol{U}}_e^{\perp} + \underset{\sim}{\boldsymbol{U}}_e^{\parallel} \tag{3}$$

Since the compatible part of the elastic distortion field $\underset{\sim}{\boldsymbol{U}}_e^{\parallel}$ is by definition curl-free, from Eq. (1) we see that the incompatible part of the elastic distortion field $\underset{\sim}{\boldsymbol{U}}_e^{\perp}$ can be simply determined from the prescribed Nye's tensor :

$$curl\ \underset{\sim}{\boldsymbol{U}}_e^{\perp} = \underset{\sim}{\boldsymbol{\alpha}} \tag{4}$$

Note that the compatible part $\underset{\sim}{\boldsymbol{U}}_e^{\parallel}$ is involved in the stress field equations to satisfy the boundary conditions and balance momentum. In the case of infinite dislocation walls, the above elasto-static field equations can be rewritten in the form of a partial differential equation of Navier-type :

$$div\ \underset{\approx}{\boldsymbol{C}} : \underset{\sim}{\boldsymbol{U}}_e^{\parallel,sym} + div\ \underset{\approx}{\boldsymbol{C}} : \underset{\sim}{\boldsymbol{U}}_e^{\perp,sym} = 0 \tag{5}$$

Since $\underset{\sim}{\boldsymbol{U}}_e^{\perp}$ must satisfy the Poisson equation, the second term in Eq. (5) can be derived from the Nye's tensor :

$$div\ \underset{\approx}{\boldsymbol{C}} : \underset{\sim}{\boldsymbol{U}}_e^{\perp} = -curl\ \underset{\sim}{\boldsymbol{\alpha}} \tag{6}$$

More details on these solutions can be found in (Acharya, 2004) and (Berbenni et al., 2014). In addition, examples of stress field calculation for different dislocation structures can be found in (Roy and Acharya, 2005) and (Fressengeas, 2017).

While the dislocation density tensor is a quantity well defined to characterize 3D polarized dislocation contents in a crystal (Kröner, 1963, Nye, 1953), the accumulation of dislocations at GBs is mathematically better characterized with a 2D singular function. This observation leads to the concept of surface dislocation density tensor (Bullough and Bilby, 1956, Mura, 1987) we can derive from the FDM theory (Acharya, 2001). When a dislocation distribution is restricted to a planar surface (interface, boundary, wall, etc.), the Nye's tensor $\underset{\sim}{\alpha}$ becomes a direct measure of the content of the continuous distribution of the Burgers vector (Bullough and Bilby, 1956). The components of the Nye's tensor are then dimensionless and that gives rise to the idea of defining a surface Nye's tensor $\underset{\sim}{\alpha}^s$. Calculation examples of surface Nye's tensor can be found in (Fressengeas, 2017, Rey and Saada, 1976).

Surface Nye's tensor can then be defined, each time a dislocation microstructure is made of dislocation segments all belonging to a given plane. Adopting the FS/RH convention, the surface Nye's tensor can be defined as Acharya (2001) :

$$\underset{\sim}{\alpha}^s = \frac{1}{S}\sum_j^n \underline{\boldsymbol{b}}_i \otimes \underline{\boldsymbol{l}}_j \tag{7}$$

where $\underline{\boldsymbol{b}}_i$, $\underline{\boldsymbol{l}}_j$ and S are the segment Burgers vector, the segment line vectors and the segment habit surface, respectively. Since the distribution of dislocations is concentrated in a wall, we adopte a solution proposed by Rey and Saada (Rey and Saada, 1976) ; a Dirac function $\delta(x)$ is used to indicate the location and orientation perpendicular to the dislocations habit plane and the dislocation density is assumed homogeneous in the latter plane.

One must differentiate three generic types of surface Nye's tensor corresponding to three model arrangements of GNDs in a wall structure (Hirth and Lothe, 1982). Those 3 arrangements are illustrated in Fig. 1 and are referenced in the following as : (a) twist walls, (b) tilt walls and (c) epitaxial walls.

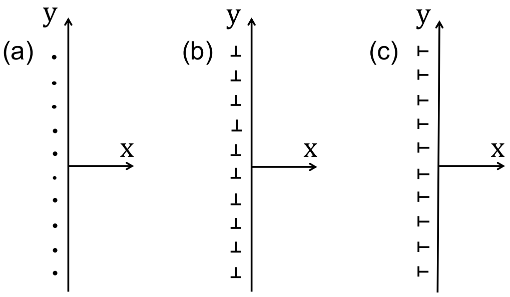

Figure 1: Schematic illustrations of the 3 types of dislocation walls considered in the following : (a) straight screw dislocations with Burgers vector in the z direction build a twist wall, (b) straight edge dislocations with Burgers vector perpendicular to the wall build a tilt wall and (c) straight edge dislocations with Burgers vector parallel to the wall build an epitaxial wall.

The first type of dislocation arrangement we consider is a "twist wall" and is sketched in Fig. 1a. It is formed of straight screw dislocations periodically spaced in a plane. The associated surface Nye's tensor has only one non-zero component. Thus, in accordance with the FDM theory, the connection between the surface Nye tensor and the incompatible part of the elastic distortion is summed up here in the simple equation :

$$\alpha^s_{zz}\delta(x) = U_{zy,x} \tag{8}$$

The integration of Eq. (8) gives the solution of the elastic distortion field through a Heaviside function :

$$U_{zy} = \int \alpha^s_{zz}\delta(x)\mathrm{d}x = \alpha^s_{zz}H(x) + A \tag{9}$$

Identification of the integration variable A in Eq. (9) requires additional assumption. It is reasonable in our case to use the Albenga's rule stating that the average of the internal stresses must vanish. In this case, the absolute values of the stresses on both sides of the wall must be the same. This condition imposes that $A = -0.5\alpha^s_{zz}$. Next, derivation of Eq. (9) provides a strain field solution and applying Hooke's law, one obtains the stresses associated with an infinite twist wall. From such calculation, we must notice that in the case of infinite twist walls, the associated stress tensor $\underset{\sim}{\sigma}$ has only two non-zero components which are proportional to the surface Nye's tensor value, hence to the surface GND density :

$$\sigma_{zy}(x \geq 0) = \sigma_{yz}(x \geq 0) = \frac{\mu}{2}\alpha^s_{zz} \tag{10}$$

with μ the crystal shear modulus. This solution satisfies the equilibrium condition div$\underset{\sim}{\sigma} = 0$.

Repeating the same calculation in the case of infinite "tilt wall" in Fig. 1b, one finds :

$$\sigma_{xy}(x \geq 0) = \sigma_{yx}(x \geq 0) = \frac{\mu}{2}\alpha^s_{xz} \tag{11}$$

Since the sign of the stress component must change when crossing the habit plane, this solution in the Heaviside form does not fulfill the equilibrium condition div$\underset{\sim}{\sigma} = 0$.

In the case of "epitaxial wall" in Fig. 1c, the non-zero component of the surface Nye tensor is this time α^s_{yz}. Following again the methodology presented above, one finds $U_{yy} = \alpha^s_{yz}/2$ and the three non-zero normal stress components :

$$\begin{aligned}
\sigma_{xx}(x \geq 0) &= \frac{\nu\mu}{(1-2\nu)}\alpha^s_{yz} \\
\sigma_{yy}(x \geq 0) &= \frac{(1-\nu)\mu}{(1-2\nu)}\alpha^s_{yz} \\
\sigma_{zz}(x \geq 0) &= \frac{\nu\mu}{(1-2\nu)}\alpha^s_{yz}
\end{aligned} \tag{12}$$

with ν the Poisson's ratio.

Similarly to the tilt wall, the stress solutions calculated for the infinite epitaxial wall are not correct. They do not fulfill equilibrium condition. The reason is that the integration scheme used in Eq. (9) does not include the compatible part of the elastic distortion. As shown by Acharya (Acharya, 2001), it happens that the compatible part does not exist in the case if the screw dislocation. This is why the solutions obtained from this equation are correct only for the screw facet. In the other cases,

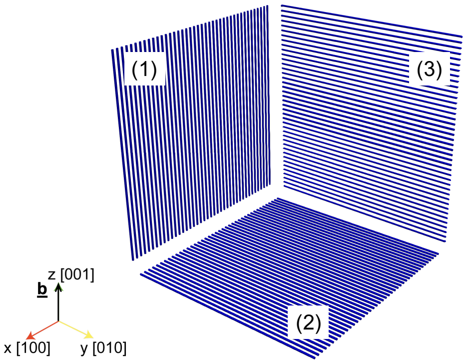

Figure 2: Schematic of the 3 GND facets tested with DD simulations. The dislocation Burgers vector $\underline{\boldsymbol{b}}$ is parallel to [001]. The 3 facets made of straight dislocation segments are lined up equidistantly and formed : (1) a twist facet, (2) a tilt facet and (3) an epitaxial facet.

these solutions will be only used as scaling factor for the fitting functions, see next chapter.
From the above calculations, we see that all the calculated stress components are constant and proportional to the surface Nye's tensor $\underset{\sim}{\alpha}^s$. A comparison between such solutions and the predictions of the dislocation theory in the case of discrete dislocation walls (Hirth and Lothe, 1982) is informative. The stress solutions derived above agree with the classical dislocation theory analysis only in the case of the infinite twist wall (Eq. (10)). Nevertheless, as it will be shown later, these solutions provide appropriate scaling for the stresses induced by finite-size walls.

3. Simulation results

3.1. Stress fields of elementary GND facets

We now characterize the stress field associated with dislocation walls having a finite height and a finite dislocation length. For the sake of clarity, this type of dislocation walls is, hereafter, referred as twist, tilt or epitaxial GND facets. A comparison is made between the previous FDM infinite solutions and the solutions calculated with the discrete dislocation dynamics (DD) simulation code *microMegas*. The main features and parameters of this code are reported in (Devincre et al., 2011).

The three different sets of GND facets considered in the simulations are schematically shown in Fig. 2. For simplicity reason, simple cubic crystal symmetry is used. The geometry and dimension of the GND facets are reported in Tab. 1 and Tab. 2, respectively.

	Twist	Tilt	Epitaxial
Burgers vector $\underline{\boldsymbol{b}}$	[001]	[001]	[001]
Plane normal $\underline{\boldsymbol{n}}$	[010]	[001]	[010]
Line direction $\underline{\boldsymbol{l}}$	[00$\bar{1}$]	[010]	[0$\bar{1}$0]

Table 1: Crystallographic definition of the three GND facets investigated with the DD simulations.

	S1	S2	S3	S4
H (μm)	10	5	10	5
L (μm)	10	5	5	10
$R = H/L$	1	1	2	0.5

Table 2: Definition of the different GND facet shapes investigated with the DD simulations. All the tested GND facets are rectangular with height noted H and width noted L. The denotation S1-S4 correspond to the facets shapes illustrated in Fig. 3.

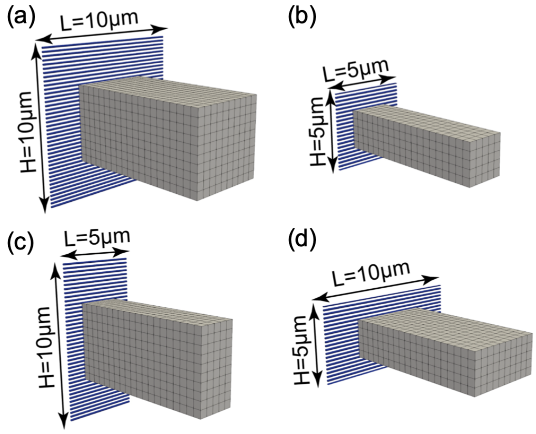

Figure 3: Four different shapes of GND facets are considered. The gray grid indicates the nodes used to calculate the average stress amplitude as a function of the facet distance. The images (a)-(d) correspond to the facets shapes S1-S4 as defined in Tab. 2.

All tested GND facets are of rectangular shapes, with two independent dimensions ; the height H and the width L. For each type of facet, different shapes and sizes were considered (see Fig. 3). In the following, the dimensionless variable R denotes the aspect ratio of the facet height H and the facet width L. To compute an average stress as a function of the distance to the facet, the stress field of the dislocations equally distributed on the facets is summed at the nodes of a 3D grid ($NX \times NY \times NZ$) parallel to the normal of the facets (Fig. 3). The height and the width of the averaging grids are by definition taken half of the tested wall height and width, respectively. The dimensions and shape of these grids have been fixed keeping in mind that we want to eventually develop the calculation of an average back-stress in the center of grains whose boundary is discretized with a small number of facets. Therefore, we limit the stress computations in a volume normal the facet, with a central axis passing through the center of each facet and lateral dimensions eliminating regions close to the facets frontiers where the stress gradient is much larger. The simulations were made using a constant surface GND density $\rho^s_{GND} = 4.1 \ 10^6$ m^{-1}. Three generic types of GND facets, illustrated with Fig. 2 are analyzed. Comparison is made with the solutions calculated in the previous section for the infinite dislocation walls.

Twist GND facets

The average stress of different twist GND facets as a function of the distance (parallel to y-axis) to the facet plane is reported in Fig. 4a. Those results are compared with the prediction of Eq. (10) for an infinite twist wall. In all the cases, only the stress component σ_{zx} is different from zero, independently of the facets dimensions and shapes. As expected for a GND finite ensemble, the amplitude of the stress is decreasing with the normal distance to the facets. In addition, we note that the stress maximum amplitude is also independent of the facet dimension and shape. This maximum is always located at $y \approx 0$ and agree with the FDM solution of Eq. (10). Hence, the maximum of the stress field profile is only function of the surface GND density.

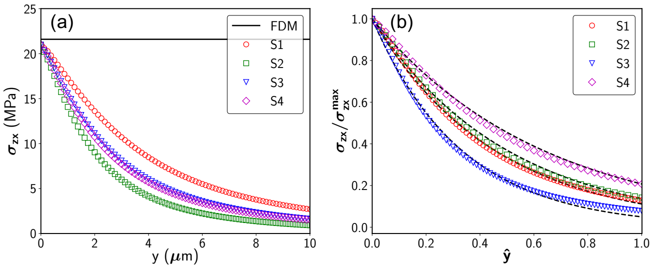

Figure 4: (a) Variation of σ_{zx} with the distance from the twist GND facets S1, S2, S3 and S4. The solid line is the FDM solution. (b) Same curves as (a) but normalized by σ_{zx}^{max} and by the facet heights H ($\hat{y} = y/H$). Dashed lines are the functions given in Eq. (13).

On the other hand, we can note in Fig. 4 that stresses induced by GND twist facets all exhibit a rapid decrease in the stress amplitude with the distance from the facet. In addition, facets with different shapes (different aspect ratio R), show different stress profiles. As illustrated in Fig. 4b, a normalization of the stress field and of the distance from the facet H does not merge the different profiles.

Tilt GND facets

The average stress of different tilt GND facets as a function of the distance (parallel to z-axis) to the facet plane are reported in Fig. 5a. Again for all tested facet shapes, only one nonzero stress component, σ_{zx}, is found. This result agrees with the infinite tilt wall solution. However, the stress profile obtained with tilt GND facets is very different from the one observed for twist GND facets. All the calculated profiles exhibit : an increase from zero stress ($z \approx 0$) up to a maximum and a decrease to zero far from the facets. The calculated maximum stress is always much smaller than the FDM solution of Eq. (11) for the infinite tilt wall.

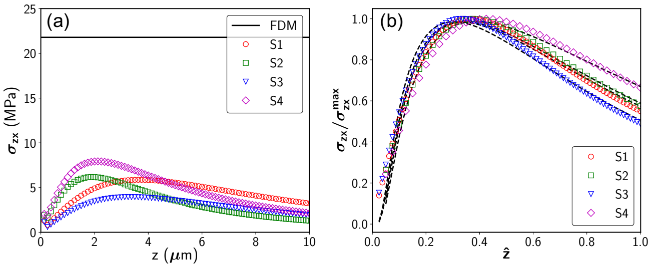

Figure 5: (a) Variation of σ_{zx} with distance for a tilt GND facet of different shapes S1, S2, S3 and S4. The solid line corresponds to the FDM solution, Eq. (11). (b) Same curves as (a) but normalized by the σ_{zx}^{max} and by the interface heights H ($\hat{z} = z/H$). Dashed lines are the functions resulting from Eq. (13).

Such stress profile with a maximum at some distance from the dislocation plane is known in the case of tilt walls made of infinite edge dislocations (Li, 1960, Saada and Bouchaud, 1993), but with a finite height. From such calculation, it was reported that the stress peak, whatever the dislocation density in the wall, always appears at a distance equal to half the wall height. Our calculations based on finite GND facets exhibit a stress peak systematically closer to the facets. For the facet shapes S1 and S3, the facets' height is $H = 10\ \mu m$ and the stress maximum is located at $z \approx 3.5\ \mu m$. For the the facet shapes S2 and S4, the facets' height is $H = 5\ \mu m$ while the stress maximum is found around $z \approx 2\ \mu m$. In addition, we note that the stress maximum increases when the dislocation length in the facets is increased. As illustrated in Fig. 5b, a normalization of the stress field profile accounting for the GND height does not standardize the results. The shape of each stress profile is then function of the shape of the facet.

Epitaxial GND facets

The simulated epitaxial GND facets have a normal axis parallel to the x-axis and are made of edge dislocations with an in-plane Burgers vector parallel to the z-axis (see Tab. 1). Unlike the tilt and twist GND facets, epitaxial facets give rise to three non-zero stress components σ_{xx}, σ_{yy} and σ_{zz} with very different profiles illustrated in Fig. 6. In brief, the normal stress component σ_{xx} has a behavior similar to the one associated with tilt facets, while the two normal stress components σ_{yy} and σ_{zz} follow the same trend as the shear stress generated by twist facets. To facilitate the discussions, we denote the stress components of epitaxial GND facets in the following order :

— The 1^{st} component is parallel to the Burgers vector $\underline{\boldsymbol{b}}$.
— The 2^{nd} component is parallel to the the plane normal $\underline{\boldsymbol{n}}$.
— The 3^{rd} component is parallel to the the dislocation line direction $\underline{\boldsymbol{l}}$.

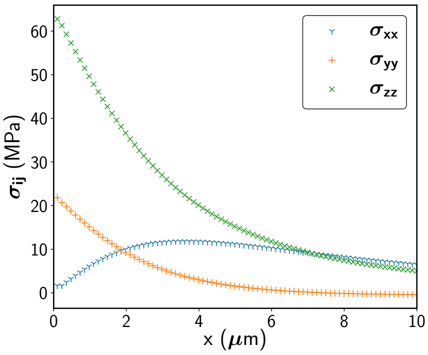

Figure 6: The three stress profiles associated with an epitaxial GND facet as function of the facet normal distance. This example corresponds to the square shape S1 of dimension 10 μm, (Tab. 2).

Stress profiles of the first component σ_{zz} calculated for different facet shapes (S1-S4) are plotted in Fig. 7a. Such stress is always maximum close to the facet plane and decreases with the distance along the x-axis. Like in the case of twist GND facets, the maximum stress of profiles is a constant value only function of the dislocation surface density and independent of the facet shape. Comparison between the solution of Eq. (12) for an infinite epitaxial wall with the same surface GND density (σ_{zz} = 179 MPa) is in poor agreement with the calculated stress σ_{zz}^{max} = 64 MPa at x = 0.

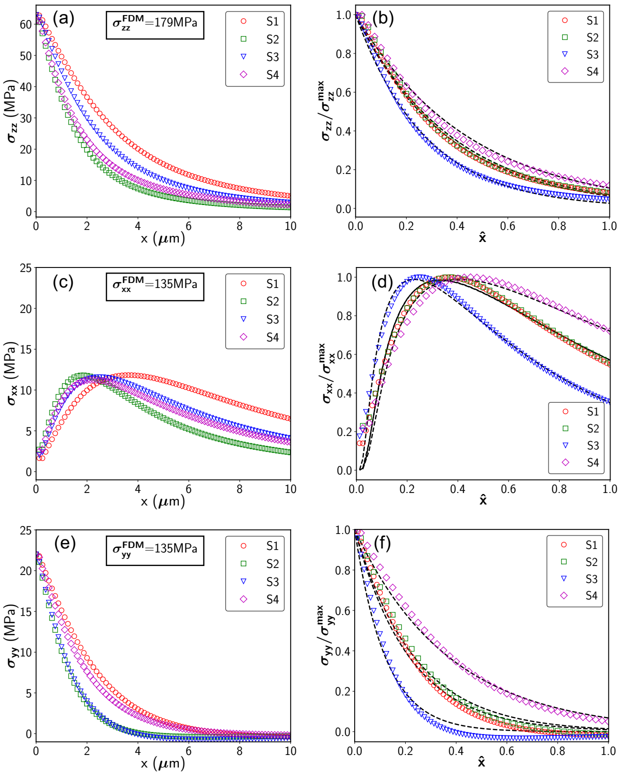

Figure 7: Variation of σ_{zz} (a), σ_{xx} (c) and σ_{yy} (e) with the distance normal to the epitaxial facets S1, S2, S3 and S4 in Tab. 2. The FDM solutions of Eq. (12) for an equivalent infinite epitaxial wall are given. (b), (d) and (f) are the same curves as (a), (c) and (e), but normalized by the maximum stress and by the facet heights H ($\hat{x} = x/H$). Dashed lines are the profiles calculated with Eq. (13).

Stress profiles of the second component σ_{xx} calculated for the different facet shapes (S1-S4) are plotted in Fig. 7c. Similar to stress variations we calculated for tilt facets, the amplitude of this stress component first increases and then decreases. The maximum stress amplitude is not influenced by the facet shape and remains a constant around $\sigma_{xx}^{max} \approx 12$ MPa. The latter value is much smaller than the solution of Eq. (12), σ_{zz}^{FDM} = 135 MPa calculated for the same surface GND density. As illustrated in Fig. 7d, a normalization of the stress field profile accounting for the height of GND facets does not standardize the results.

Stress profiles of the third component σ_{yy} calculated for the different facet shapes (S1-S4) are plotted in Fig. 7e. Variations of this stress component are very close to σ_{zz}. A maximum stress amplitude is found close to the facets and the stress amplitude decreases with the distance along the x-axis. The calculated maximum stress (much smaller than Eq. (12) solution) is constant and is independent of the facet shape.

3.2. Tailoring the FDM solutions

In the previous sections, we showed that the analytical expressions (Eqs. 10-12) derived from the FDM theory provide appropriate scaling for the stress profiles and allow identification of the non-zero stress components. It is thus possible to empirically adjust the computed profiles. Such adjustment procedure is carried out in two steps. We first determine, a scaling factor F that relates the σ^{FDM} solution to the maximum stress computed in DD σ^{max}. Then, a shape function ξ is identified for each non-zero component of the stress field. This shape function provides a quantitative description of the stress variation profile with respect to the normal distance to the facet. At last, the stress profile $\sigma(\hat{x})$ of a given GND facet could be formulated like :

$$\sigma(\hat{x}) = F\sigma^{FDM}\xi(\hat{x}) \tag{13}$$

with $\hat{x}$ the true distance x from the facet center normalized by the facet height H ($\hat{x} = x/H$).

Identification of the scaling factors F

The analysis made in the previous section supports the idea that different scaling factors F must exist for the three different types of GND facets, i.e., twist, tilt and epitaxial GND facets.

As illustrated in Fig. 4, the amplitude of σ^{max} calculated with all tested twist facets is constant and equal to the FDM prediction in Eq. (10). Hence, in the twist facet case the scaling factor is simply $F_{tw} = 1$.

For the tilt facets the computed σ^{max} value is found to change with the facet shape (see Fig. 5a). Nevertheless, when calculating the ratio ($\sigma^{max}/\sigma^{FDM}$), it becomes clear that the scaling factors F_{ti} follows a simple geometrical rule which is a function of the aspect ratio of facets R :

$$F_{ti}^{calc} = 1/\left[2(1+R)\right] \tag{14}$$

In Tab. 3, the computed and calculated scaling factors predicted from Eq. (14) are summarized for tilt facets of different shapes and a good agreement is found between F_{ti} and F_{ti}^{calc}.

Facet shape	F_{ti}	$R = H/L$	F_{ti}^{calc}
S1	0.25	1	0.25
S2	0.26	1	0.25
S3	0.17	2	0.17
S4	0.35	0.5	0.33

Table 3: Identification of the scaling factor accounting for the tilt facets. F_{ti} is the scaling factor estimated from the simulation results reported in Fig. 5a. R is the aspect ratio of the tilt facets shown in Fig. 3. F_{ti}^{calc} is the calculated scaling factors using Eq. (14).

Lastly, the analysis of the epitaxial facets simulations reported in Fig. 6 leads to two main conclusions : a) three scaling factors must be defined for the three non-zero stress components identified for the epitaxial facets. b) like in the case of twist facets, such scaling factors are constants since σ^{max} is unchanged when changing the shape of the facets. Hence, following the stress component order defined in the previous section, we identified : $F_{ep1} = 0.36$, $F_{ep2} = 0.09$ and $F_{ep3} = 0.16$.

Identification of the shape functions ξ

Analysis of the stress profiles reported in Figs. 5-7 suggest that only two shape functions denoted ξ_1 and ξ_2 are necessary to reproduce all the simulated stress profiles. The first shape function $\xi_1(\hat{x})$ is a one-parameter function which allows describing a monotonous decrease of the stress field as a function of $\hat{x}$:

$$\xi_1(\hat{x}) = \exp(-a\hat{x}) \tag{15}$$

The second shape function $\xi_2(\hat{x})$ is a two parameters function describing concave stress profiles with a maximum value at some distance from the GND facets :

$$\xi_2(\hat{x}) = \exp\left[-\frac{(\hat{x}-a)^2}{b\hat{x}}\right] \tag{16}$$

in the two above equations, a and b are parameters whose variations for each type of GND facets in different shapes can be identified from the DD simulation results reported in Figs. 5-7.

In the case of twist facets, the parameter a_{tw} appearing in the shape function is found to vary linearly with the aspect ratio R and takes the form :

$$a_{tw} = 1.1 + 0.95R \tag{17}$$

In the case of the tilt facets, the two parameters involved in the shape function (Eq. (16)) are also found to vary linearly with the aspect ratio. They take the simple forms :

$$a_{ti} = 0.4 - 0.05R \quad \text{and} \quad b_{ti} = 1 - 0.15R \tag{18}$$

In the case of the epitaxial facets and following the remarks made in the previous section, two cases must be differentiated. The modeling of components σ_{zz} and σ_{yy}, involves shape function with only one fitting parameter (see Fig. 7b and f). Like in the case of twist facets, the calculated solutions for the parameter a for both stress components are found to vary linearly with the aspect ratio R and they take the form :

$$a_{ep1} = 1.8 + 0.9R \tag{19a}$$

$$a_{ep3} = 3.6 + 0.8R \tag{19b}$$

Alternatively, the profile of σ_{xx} associated with epitaxial facets exhibits a peak (see Fig. 7d) and therefore involves a shape function with two parameters. Fitted results of those two parameters give again a linear function of the aspect ratio R :

$$a_{ep2} = 0.46 - 0.12R \quad \text{and} \quad b_{ep2} = 1.2 - 0.33R \tag{20}$$

The relevance of the chosen shape functions and the quality of the fitting process can be checked in Figs. 4b, 5b and 7(b,d,f).

The effect of the GND density

In order to test the proportionality between the stress and the GND density predicted by the FDM theory, additional simulations with different GND density in facets of square shape (S1) were performed (see Fig. 8), using the three generic types of dislocation walls, i.e. twist, tilt and epitaxial characters.

The stress profiles of these 9 simulations were then fitted using the same adjustment procedure as described above. The identified parameters are given in Tab. 4 and can easily be compared to the solutions given by Eqs. 17, 18, 19a, 19b and 20.

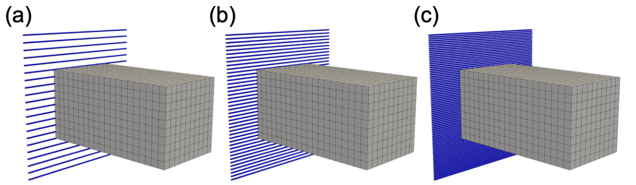

FIGURE 8: GND facets of shape S1 (see Tab. 2) are simulated with an increasing number of equally spaced dislocation lines. The corresponding surface GND density are (a) $\rho^s_{GND} = 2.1\ 10^6\ \mathrm{m}^{-1}$, (b) $\rho^s_{GND} = 4.1\ 10^6\ \mathrm{m}^{-1}$ and (c) $\rho^s_{GND} = 8.1\ 10^6\ \mathrm{m}^{-1}$.

$\rho^s_{GND}\left(10^6\ m^{-1}\right)$	F_{tw}	a_{tw}	F_{ti}	a_{ti}	b_{ti}	F_{ep1}	a_{ep1}	F_{ep2}	a_{ep2}
2.1	1	2.28	0.25	0.34	0.85	0.36	2.70	0.09	0.33
4.1	1	2.19	0.25	0.33	0.82	0.36	2.74	0.09	0.33
8.1	1	2.20	0.25	0.33	0.81	0.36	2.76	0.09	0.33

TABLE 4: Identification of the scaling factors F and the parameters in shape functions $\xi(\hat{x})$ for twist, tilt and epitaxial facets with shape S1 for an increasing surface GND density ρ^s_{GND}.

From those calculations it is apparent that all the parameters identified in the previous section are precisely recovered. We observe no significant variations of these parameters when changing ρ^s_{GND}. These results validate the empirical approach we proposed and confirm that the long-range stress field associated with GND facets is proportional to the surface GND density.

3.3. Accounting for crystal structure

The dislocation distributions and configurations used in the previous section were of simple cubic symmetry. In real crystals, the dislocations accumulated at GBs are mostly of mixed character and the dislocation glide planes intersect the GBs at any angles. Therefore, the surface Nye's tensor $\underset{\sim}{\alpha}^s$ calculated at a GBs may have up to nine non-zero components. The solution we propose to account for such complexity is as follows. For the sake of simplicity, we consider a coordinate system in which the GB is perpendicular to one of the cubic axis. In this system, the GND tensor must have at least three zero components whose line direction is out of the GB plane. Similarly to the well-known vector decomposition of the mixed dislocation into an edge and a screw components, we can consider that every component of a surface GND tensor corresponds to the surface density of a virtual set of GNDs belonging to one of the three elementary GND characters introduced in the last section, i.e., twist, tilt and epitaxial. For example, consider a grain boundary containing a homogeneous distribution of dislocations of one mixed character inducing three components in the Nye tensor. These components correspond to three virtual GND density of the three elementary characters. From a mechanical point of view, the stress induced by such configuration is equivalent to the sum of the stress tensors induced by every component of the Nye tensor. This vector decomposition is possible due to the proportionality between the stress and the Nye tensor components.

Consequently, the stress induced by GNDs on every facet can be determined no matter their character. If the contributions of every facet of the grain are added, the internal stresses at the grain center can be determined.

$\underset{\sim}{\alpha}^s$	$\underline{\boldsymbol{b}}_s$	$\underline{\boldsymbol{l}}_s$	x	y	z
α^s_{xx}	[100]	[100]	–	Twist	Twist
α^s_{xy}	[100]	[010]	Tilt	–	Epitaxial
α^s_{xz}	[100]	[001]	Tilt	Epitaxial	–
α^s_{yx}	[010]	[100]	–	Tilt	Epitaxial
α^s_{yy}	[010]	[010]	Twist	–	Twist
α^s_{yz}	[010]	[001]	Epitaxial	Tilt	–
α^s_{zx}	[001]	[100]	–	Epitaxial	Tilt
α^s_{zy}	[001]	[010]	Epitaxial	–	Tilt
α^s_{zz}	[001]	[001]	Twist	Twist	–

Table 5: Projection of the surface Nye's tensor $\underset{\sim}{\alpha}^s$ components on the simple cubic symmetry. The Burgers vector $\underline{\boldsymbol{b}}_s$ and dislocation line vector $\underline{\boldsymbol{l}}_s$ are indicated. The character of each component in surface Nye's tensor is specified for three possible configurations with facet normal along x, y and z axis. The symbol "–" is associated with the null component of $\underset{\sim}{\alpha}^s$. Those null components exist because there is no GND density out of the facet's plane.

The one-to-one correspondence between Nye's tensor components and dislocation configurations that can be reconstructed with the simple cubic symmetry reported in Tab. 5. As an example of calculation, the case of a GND facet in a crystal with FCC symmetry and containing one type of mixed dislocations is presented (see Fig. 9a). The size of the tested facet is 10 μm. The facet plane is normal to z-axis and contains mixed dislocations of Burgers vector parallel to $1/\sqrt{2}[101]$ and line direction parallel to $1/\sqrt{2}[110]$, equidistantly distributed. The tested surface GND density is $\rho^s_{GND} \simeq 5\ 10^6\ \mathrm{m}^{-1}$. The resulting surface Nye's tensor $\underset{\sim}{\alpha}^s$ associated with such facet is thus :

$$\underset{\sim}{\alpha}^s = \begin{pmatrix} \alpha^s_{xx} & \alpha^s_{xy} & 0 \\ 0 & 0 & 0 \\ \alpha^s_{zx} & \alpha^s_{zy} & 0 \end{pmatrix} = \rho^s_{GND} \frac{||\underline{\boldsymbol{b}}||}{2} \delta(z) \begin{pmatrix} 1 & 1 & 0 \\ 0 & 0 & 0 \\ 1 & 1 & 0 \end{pmatrix} \quad (21)$$

where $||\underline{\boldsymbol{b}}|| \approx 2.55\ 10^{-10}\ m$ the norm of Burgers vector for copper and $\delta(z)$ is the Dirac distribution function. In concordance with our calculation procedure, this GND facet is decomposed as follows. The component α^s_{xx} is attributed to a twist facet with screw dislocations having $\underline{\boldsymbol{b}}_s = [100]$ and $\underline{\boldsymbol{l}}_s = [100]$. The component α^s_{xy} is attributed to an epitaxial facet with edge dislocations having $\underline{\boldsymbol{b}}_s = [100]$ and $\underline{\boldsymbol{l}}_s = [010]$. The last two components α^s_{zx} and α^s_{zy} are attributed to tilt facet configurations with edge dislocations having $\underline{\boldsymbol{b}}_s = [001]$ and $\underline{\boldsymbol{l}}_s = [100]$ and $\underline{\boldsymbol{b}}_s = [001]$ and $\underline{\boldsymbol{l}}_s = [010]$, respectively. This decomposition is part of a general solution we summarized in the Tab. 5 for all GND facets with normals parallel to axis x, y or z. Here it must be noted that the same procedure can be applied to any facet orientation with the help of additional rotation operations that spin the facet to a reference basis defined with x, y and z axis.

Comparison is made in Fig. 9b between DD simulations results (open marks) and calculations (doted lines) based on the decomposition procedure defined in the Tab. 5 and the solutions of Eq. (13) for tilt, twist and epitaxial GND facets. A systematic analysis of this calculation shows that the component α^s_{xx} induces the stress σ_{xy}, the component α^s_{xy} is at the origin of the three normal stress σ_{xx}, σ_{yy} and σ_{zz} and the components α^s_{zx} and α^s_{zy} induce the shear stress σ_{yz} and σ_{xz}, respectively. Comparing the calculated solutions and the DD simulation results, an excellent agreement is found for each stress component. An error, about 25%, exists only close to the facet and on the two stress components σ_{xx} and σ_{yy}. This error is considered in the following as acceptable since we are interested in the stress prevailing in the bulk of the grain, i.e., at some distance from GB facets.

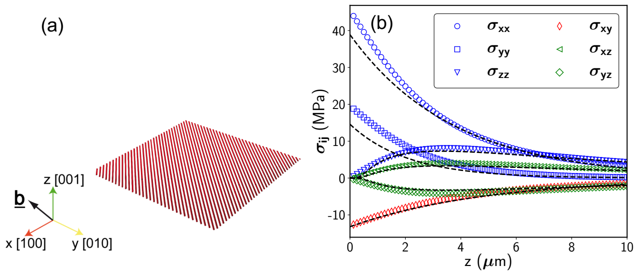

Figure 9: Example of stress calculation for a [001] facet made of mixed dislocations of slip system $1/\sqrt{2}[101]$. The size of the present facet is $10 \times 10\ \mu m$ and the surface dislocation density is $\rho^s_{GND} \simeq 5\ 10^6 m^{-1}$. (a) The [001] facet with mixed FCC dislocations ($\underline{\boldsymbol{b}}$ parallel to [101] and line direction $\underline{\boldsymbol{l}}$ parallel to [110]), (b) the full stress tensor as a function of the distance z to the interface. Open symbols refer to the stress computed with DD simulations and the dashed lines correspond to the predictions made with the simple cubic symmetry decomposition.

4. Predicting internal stresses inside grains

In this section, a strategy to rapidly evaluate the internal stress inside grains with surface GND density deposited at the GBs is presented. The validation of the calculation is made with comparisons to DD simulations in static and dynamic conditions.

4.1. Static validation tests

To test the reliability of the calculation procedure, DD simulations were used to explore different GND configurations with increasing complexity. GND configurations are prepared by DD simulations using cubic grains with the FCC symmetry. The grain dimension is 10 μm and the GBs are impenetrable to dislocations. Then we impose the expansion of dislocation sources inside the grains to pave the GBs. Four static configurations are tested in the following. First, three configurations made of one grain embedded in an elastic infinite matrix are illustrated in Fig. 10a-c. In the configuration (a) 100 dislocation loops of the same slip system are uniformly distributed at the GBs, (b) 150 dislocation loops taken from three non-parallel slip planes are uniformly distributed at the GBs and (c) a GND microstructure made of 100 dislocation loops of the same slip system are randomly distributed at the GBs. Lastly, as illustrated in Fig. 10d, a periodic polycrystal aggregate made of four cubic grains was tested. This aggregate configuration includes two grains having a GND microstructure built with 100 randomly distributed dislocation loops of one slip system and two grains having a GND microstructure built with 150 randomly distributed dislocation loops of 3 non-parallel slip systems.

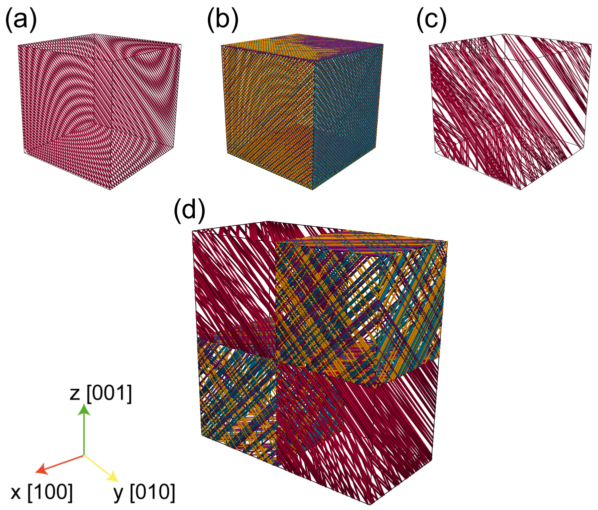

FIGURE 10: Four different static GND microstructures assembled with DD simulations are used to test the internal stress calculation procedure. The dimension of each single cubic grain is 10 μm.

Details on each GND configuration are given in the text.

Two intermediate calculations between the unique facet problem presented in Fig. 9 and the more complex calculations accounting for several facets presented in Fig. 10 are made. These calculations correspond to the stress associated with a [001] facet taken from the configurations Fig. 10(b and c). The obtained stress profiles with the distance to the facet are shown in Fig. 11. In both cases, the stress prediction (in dashed lines) is in good agreement with the stress profile computed from the DD simulations. The maximum discrepancy is systematically observed close to the facets. The comparison between Fig. 9b and Fig. 11b emphasizes the effect of uneven dislocation spacing which introduces second order errors in the calculation mostly observed close to the dislocations plane.

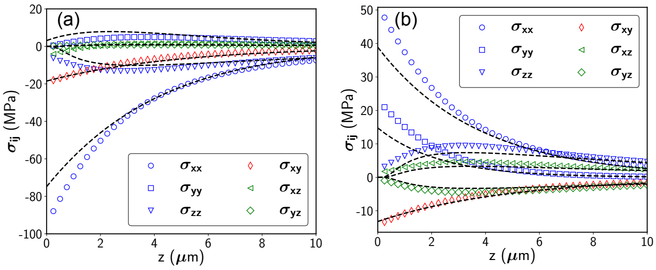

FIGURE 11: Stress calculation for a [001] facet extracted from the grain configurations illustrated in Fig. 10b and Fig. 10c. The facets dimensions are 10 × 10 μm. (a) The facet used for this stress calculation is made of approximately 100 mixed dislocations taken from three non-parallel slip systems and uniformly distributed, (b) The facet used for this calculation is made of approximately 70 mixed dislocations taken from the same slip system ($\underline{\boldsymbol{b}}$ parallel to [101] and line direction $\underline{\boldsymbol{l}}$ parallel to [110]) and randomly distributed. Open symbols refer to the stress computed with DD simulations and the dashed lines correspond to the predictions made with the simple cubic symmetry decomposition.

The inner area of the grains in the four tested configurations reproduced in Fig. 10 is dislocation free. In the case (a-c), the stress inside grains is uniquely associated with the surface GND density accumulated at GBs. In the case (d), the stress inside the four grains is computed using the 6 bounding facets and for each facet the dislocations accumulated on both sides are taken into account. It is then straightforward to calculate the internal stress at grain center with the approach presented above (τ^{calc}) and to compare it with the DD simulations solution (τ^{DD}). τ^{calc} and τ^{DD} are the resolved shear stress calculated on the slip system considered inside the grains. τ^{DD} is the average stress computed at the center of the simulated grain in a volume of 5×5×5 μm. The relative error between τ^{calc} and τ^{DD} is estimated at the grain center using $E = \|(\tau^{calc} - \tau^{DD})/\tau^{DD}\|$. When several slip systems are activated inside a grain, the prediction error E is taken as the average of the different errors. In the aggregate computation, the prediction error E is taken as the average of the 4 grains calculations. The relative errors of all the tested GND microstructures (listed in Fig. 10a-d) are summarized in Tab. 6. In addition to the relative error E estimated at the center of grain, a supplementary calculation is made to evaluate the maximum error throughout the whole inner area of grain using $E_{max} = \|(\tau^{calc}_{max} - \tau^{DD})/\tau^{DD}\|$. As we can see from Fig. 9b, the stress prediction for a given GB facet is in good agreement with the stress profile computed by DD simulations, however a minor discrepancy exhibits when the distance to the GB facet is shorter than ≈ 3 μm. As exepected, the region close to the GBs is the place where the maximum errors is identified whatever the tested cases. The E_{max} value calculated for each case are summarized in Tab. 6.

	(a)	(b)	(c)	(d)
E	3%	5%	8%	15%
E_{max}	7%	15%	20%	23%

TABLE 6: Relative errors E and maximum errors E_{max} between the calculated and simulated resolved shear stress for the four GND microstructures illustrated in Fig. 10.

Overall, the maximum calculation errors are observed in the GBs vicinity and is not representative of the state of internal stress we want to evaluate at grains center. Calculated stress at grain center is found to be in good agreement with DD simulation results for the three grains (a-c), with an error less than 10%. Hence, one can conclude that the calculation approach we proposed is quite efficient in predicting the stress induced by a uniform and a random distribution of polarized dislocations deposited at GB facets. The prediction precision is, as expected, nearly unchanged when the number of slip systems inside the grains is multiplied (a to b). However, we note that the calculated error increases from 3 to 8% when the distribution of surface GNDs becomes non-uniform (a to c).

In the last case of the periodic four-grain aggregate (d), it must be noted that dislocations belonging to different slip systems are now accumulated on both sides of the GBs between the adjacent grains. Therefore, the total GND density located at the GB facets and used to calculate the internal stress at the grain center is made of several slip systems accumulated on both sides of the GBs. The averaged relative error in the four grains of aggregate is 15% (see Tab. 6). A more detailed analysis of this calculation shows that such error is mostly associated with the heterogeneous distribution of the GNDs accumulated at the GBs facets. The calculation discrepancy is significantly reduced when considering a more regular distribution of surface GNDs at GBs.

4.2. Dynamic validation test

We now explore the possibility to use the decomposition methodology described in § 3.3 to calculate the internal stress or "back stress" during the plastic deformation in a grain and to predict stress-strain behavior. To explore such possibility, a tensile test is reproduced with a DD simulation. We plastically deform a cubic grain of copper with size 10 μm and embedded in an infinite elastic matrix. The tensile axis is orientated to deform the grain in single slip condition and like in the previous simulations GBs are defined as impenetrable interfaces. The simulation starts with a homogeneous distribution of Frank-Read sources of length 3 μm inside the grain, equivalent to density $\rho_{ini} = 5\ 10^{11}\ \mathrm{m}^{-2}$. The simulated deformation is stopped at $\varepsilon_p = 0.2\%$, i.e., before a strong localization of the plastic deformation is observed inside the grain.

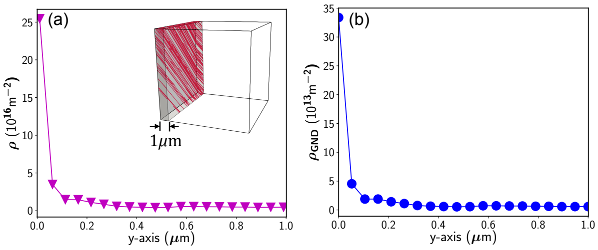

Figure 12: (a) *Average* distribution of the dislocation density ρ and (b) the scalar GND density ρ_{GND} displayed with the distance to the GB normal to y-axis. The definition of ρ_{GND} is derived from a norm of Nye's tensor $||\alpha_{ij}||$ divided by Burgers vector b (see Eq. (22)). Both calculations are made using sampling layers 0.05 μm thick.

The evolution of the dislocation density ρ inside the grain as a function of the distance from the GB is tracked during the computations and the last profile we have at the end of the simulation is plotted in Fig. 12a. For such calculation, the dislocation density is computed in layers of 0.05 μm thick parallel to the GB. The dislocation density calculated close to the GB is extremely high and then decreases rapidly to a plateau value of the density. A ratio of about 20 exists between the dislocation density found in the vicinity of the GBs and in the grain bulk. Not shown in Fig. 12a, we checked that beyond the 1 μm region, the dislocation density remains almost constant and is not polarized.

In case of simple cubic materials, a one-to-one correspondence exists between the components of Nye's tensor and the scalar GND density defined in an appropriate reference frame (Arsenlis and Parks, 1999b, Sun et al., 2000). A norm of Nye's tensor can then be defined to simply shows the proportionality between Nye's tensor and the GND bulk density (El-Dasher et al., 2003, Pantleon, 2008) :

$$\rho_{GND} = \frac{1}{b} \sum_i \sum_j ||\alpha_{ij}|| \tag{22}$$

For comparison, the profile of a scalar GND density ρ_{GND} is shown in Fig. 12b. As expected, the profile of ρ_{GND} is very close to the dislocation density profile. The magnitude of ρ_{GND} abruptly decreases and goes to zero once moving away from the GB. This result confirms that the concentration of dislocation density accumulated close to the GBs is mostly composed of GND while the much lower density of dislocations found inside the grain is made of SSD.

However, it is not simple to define the transition distance between the region close to the GBs composed of GND and the grain inner area without GND. An empirical approach is proposed to determine such frontier. First, the ρ_{GND} distribution shown in Fig. 12b is normalized by the maximum value of ρ_{GND} computed in the closest vicinity of GB. Then, we calculate the derivative of this normalized ρ_{GND} to evaluate the decreasing trend of ρ_{GND}. When the layer thickness approaches to 0.4 μm, the derivative becomes lower than 0.1%. From this result and other analyses we made for different simulation geometry, we consider that, at plastic deformation lower or equal to 0.2%, the GND density, which is accumulated within the grains, is mostly stored in a region of 0.4 μm thick close to the GBs. Such DD simulation result is in agreement with many experimental results. For instance, highly polarized dislocation density was recently observed by TEM in a thin area of 0.18 μm thick close to the lath boundaries in bainitic steels at yield (He et al., 2018).

Therefore, two regions inside the grain must be differentiated. One, the GBs region contains a large amount of dislocation most exclusively made of GND. The rest of the grain bulk contains a much lower dislocation density essentially made of forest dislocations or SSD. Hence, it must be noted that in DD simulations the evolution of both SSD and GND density can simply be tracked by monitoring two different regions. Such density can then be used to make a prediction of the internal stress inside the grain during plastic deformation. First, the calculation of the SSD density ρ_{SSD} in the central volume of the grain with the Taylor equation is used to evaluate the forest strengthening, $\tau_f = 0.35\mu b\sqrt{\rho_{SSD}}$. Second, the long-range stress τ_{GND} introduced by the accumulation of GND at GBs is determined inside the grain (at the grain center) with the calculation procedure developed above. In brief , we compute the surface Nye's tensor associated with each GB facet. Then, we calculate the corresponding internal stress tensor. Such calculation is repeated for all 6 bounding facets. At last, we sum up the solution of the internal stress tensors calculated at the grain center and resolve such stress tensor on the most active slip system to evaluate τ_{GND}. The magnitude of the two hardening mechanism being very different, the flow stress inside grains is possibly defined as a simple superposition of τ_f and τ_{GND}. A validation of this calculation procedure is presented in Fig. 13 based on a comparison with the stress-strain curve directly computed from DD simulation.

In Fig. 13, the green and the orange areas show the contribution of τ_f and τ_{GND} calculated respectively from the forest dislocations and the GND density monitored during the simulation. A slight increase is observed in τ_f because forest dislocation density did not evolve significantly with the simulated plastic deformation. The long-range stress τ_{GND} associated with the surface GND density (calculated in a region of 0.4 μm thick close to GBs) is identified at the grain center by assembling the contributions of the 6 GB facets following the procedure defined in the previous sections. The large increase of τ_{GND} observed is related to the rapid accumulation of GND at GBs with plastic strain. From such calculation, one can conclude that a linear superposition of τ_f and τ_{GND} gives a relatively good prediction of the simulated stress-strain curve. Also, we see that the contribution of τ_{GND} to the flow stress is about 80% and is responsible for most of the strain hardening. In other words, strain hardening in a confined grain mainly arises from the long-range stress generated by the GND density accumulated at GBs. Still, our calculation underestimates the simulated stress-strain curve by a few percents. This error comes mostly from the calculation of τ_{GND}. Indeed, the calculation approach we proposed is assuming a homogeneous density of GND at GBs facets, when the DD simulations reproduce some inhomogeneity of such quantity. This problem is critical in the DD simulations of cubic grains we explore in the present study since very few dislocations can, for geometrical reason, visit the grain corners during plastic deformation.

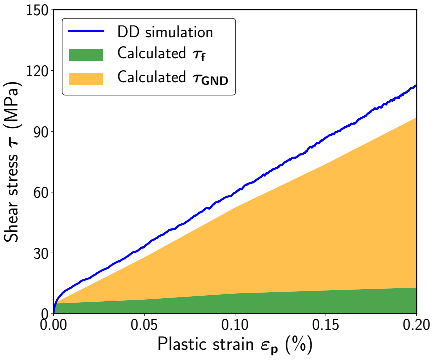

Figure 13: Comparison between the stress-strain (blue line) simulated with a cubic grain (10 μm) embedded inside an elastic matrix and the predictions of the forest and GND strengthening amplitude with the plastic strain. τ_f in green is the short-range internal stress associated with forest dislocations density calculated in central volume of the grain and from the Taylor equation. τ_{GND} in orange is the long-rang stress evaluated at the grain center with the calculation method proposed in this paper. The surface GND density extracted from DD simulation is evaluated from solid slice 0.4 μm thick on the GBs.

5. Concluding remarks

With the help of DD simulations, we show that at low plastic strain, the accumulation of GND in crystal grains is essentially localized in the close vicinity of GBs. The observed GND microstructure is confined to very thin regions and therefore can be approximated with a 2D planar distribution of dislocations named as GND facets. To calculate the long-range stress field associated with such GND facets a new approach based on the Field Dislocations Mechanics (FDM) results has been developed. Indeed, the FDM theory provides a simple solution to calculate the stress field associated with infinite walls of dislocations based on the concept of surface Nye's tensor.

In order to identify a general solution for the calculation of the stress profile of GND facets, dislocation character, dislocation density and facet shape are systematically investigated using DD simulations. From such simulations, we show that the combination of three generic types of GND facets, i.e., twist, tilt and epitaxial facets, allows for the calculation of the stress field profile associated with any type of GND network at GB. More precisely, the analytical solution we proposed for the three generic types of GND facets make use of the FDM solutions for infinite dislocation walls modified with 2 parametric functions fitted with DD simulation results. The first term is a scaling factor F that rescale the FDM solutions to the exact stress amplitude calculated in the DD simulations. The second term is a shape function $\xi(\hat{x})$ capturing the stress variation with the distance from the facet. Finally, the stress field associated with any GB facets can be calculated by superposing the stress contribution of elementary facet solutions that are identified from the surface Nye's tensor at the GB facet.

With the above procedure, the stress at the center of regular grains is calculated as the sum of the stress contributions from the GND facets bounding the grain. Such calculation was tested on several sets of DD simulations made with simple FCC grains. The cases of uniform, random and heterogeneous GND distribution in single and multiple slip conditions in periodic grains and aggregates are all considered. The comparison between the internal stress directly computed in the DD simulations and the one calculated with the facet decomposition gives confidence in the empirical calculation procedure proposed. Irregular distribution of GND at GBs is the main cause of the discrepancy between the two calculations. This source of error is thought to be acceptable at low plastic strain.

The model configurations we investigated in the present study are far from being representative of real polycrystals, still they reveal an essential feature of crystal plasticity. At low strain, when GBs are strong barriers to dislocation glide, the grain mechanics can be reproduced with simple dislocation density models and the strengthening mechanism taking place during plastic deformation can be evaluated analytically with continuous models. A prediction of the flow stress inside grains requires 2 independent calculations for the short- and long-range stress contributions, i.e., the contribution of the SSD and GND density. In the present study, an original and numerically efficient procedure is presented to calculate the internal stress associated with GND density. Future work will focus on exploiting this computational procedure for finite element modeling of crystal plasticity.

Acknowledgment

This work was partially funded from the Euratom research and training program 2014-2018 under grant agreement No 661913 (SOTERIA). This work also contributes to the Joint Program on

Nuclear Materials (JPNM) of the European Energy Research Alliance (EERA).

References

A. Acharya. A model of crystal plasticity based on the theory of continuously distributed dislocations. *J. Mech. Phys. Solids*, 49(4) :761–784, 2001.

A. Acharya. Driving forces and boundary conditions in continuum dislocation mechanics. *Proceedings of the Royal Society A : Mathematical, Physical and Engineering Sciences*, 459, 06 2002.

A. Acharya. Constitutive analysis of finite deformation field dislocation mechanics. *J. Mech. Phys. Solids*, 52 :301–316, 02 2004.

E. Aifantis. Strain gradient interpretation of size effects. *Int. J. Fract.*, 95 : 299–314, 1999.

Y. Amouyal, E. Rabkin, and Y. Mishin. Correlation between grain boundary energy and geometry in Ni-rich NiAl. *Acta Mater.*, 53(14) :3795–3805, 2005.

A. Arsenlis and D. Parks. Crystallographic aspects of geometrically-necessary and statistically-stored dislocation density. *Acta Mater.*, 47(5) :1597–1611, 1999a.

A. Arsenlis and D. M. Parks. Crystallographic aspects of geometrically-necessary and statistically-stored dislocation density. *Acta Materialia*, 47 (5) :1597–1611, 1999b.

M. Ashby. The deformation of plastically non-homogeneous materials. *Philos. Mag.*, 21(170) :399–424, 1970.

S. Berbenni, V. Taupin, K. S. Djaka, and C. Fressengeas. A numerical spectral approach for solving elasto-static field dislocation and g-disclination mechanics. *International Journal of Solids and Structures*, 51(23) :4157–4175, 2014. doi : https://doi.org/10.1016/j.ijsolstr.2014.08.009.

S. Berbenni, V. Taupin, and R. Lebensohn. A fast fourier transform-based mesoscale field dislocation mechanics study of grain size effects and reversible plasticity in polycrystals. *J. Mech. Phys. Solids*, 135 :103808, 2020.

R. Bullough and B. Bilby. Continuous Distributions of Dislocations : Surface Dislocations and the Crystallography of Martensitic Transformations. *Proc. Phys. Soc. Sect. B*, 69(12) :1276–1286, dec 1956.

F. Caballero, H.-W. Yen, M. Miller, J.-R. Yang, J. Cornide, and C. Garcia-Mateo. Complementary use of transmission electron microscopy and atom probe tomography for the examination of plastic accommodation in nanocrystalline bainitic steels. *Acta Mater.*, 59(15) :6117–6123, 2011.

M. Calcagnotto, D. Ponge, E. Demir, and D. Raabe. Orientation gradients and geometrically necessary dislocations in ultrafine grained dual-phase steels studied by 2D and 3D EBSD. *Mater. Sci. Eng. A*, 527(10-11) :2738–2746, 2010.

Z. Cheng, H. Zhou, Q. Lu, H. Gao, and L. Lu. Extra strengthening and work hardening in gradient nanotwinned metals. *Science*, 362(6414), 2018.

N. Cordero, S. Forest, E. Busso, S. Berbenni, and M. Cherkaoui. Grain size effects on plastic strain and dislocation density tensor fields in metal polycrystals. *Comput. Mater. Sci.*, 52(1) :7–13, 2012.

B. Devincre, R. Madec, G. Monnet, S. Queyreau, R. Gatti, and L. Kubin. Modeling crystal plasticity with dislocation dynamcis simulations : The "microMEGAS" code. In A. P. S. Forest, editor, *Mech. Nano-Objects*, pages 81–100. Presses des Mines, 2011.

A. Dubinko, D. Terentyev, A. Bakaeva, K. Verbeken, M. Wirtz, and M. Hernández-Mayoral. Evolution of plastic deformation in heavily deformed and recrystallized tungsten of ITER specification studied by TEM. *Int. J. Refract. Met. Hard Mater.*, 66 :105–115, 2017.

B. El-Dasher, B. Adams, and A. Rollett. Viewpoint : experimental recovery of geometrically necessary dislocation density in polycrystals. *Scripta Materialia*, 48(2) :141 – 145, 2003.

X. Feaugas. On the origin of the tensile flow stress in the stainless steel AISI 316L at 300 K : Back stress and effective stress. *Acta Mater.*, 47(13) :3617–3632, 1999.

N. Fleck, G. Muller, M. Ashby, and J. Hutchinson. Strain gradient plasticity : Theory and experiment. *Acta Metall. Mater.*, 42(2) :475–487, 1994.

N. Fleck, M. Ashby, and J. Hutchinson. The role of geometrically necessary dislocations in giving material strengthening. *Scr. Mater.*, 48(2) :179–183, 2003.

C. Fressengeas. *Mechanics of Dislocation Fields*. Wiley-ISTE, 2017.

H. Gao and Y. Huang. Geometrically necessary dislocation and size-dependent plasticity. *Scr. Mater*, 48 :113–118, 2003.

H. Gao, Y. Huang, W. Nix, and J. Hutchinson. Mechanism-based strain gradient plasticity— I. Theory. *J. Mech. Phys. Solids*, 47(6) :1239–1263, 1999.

J. Gibeling and W. Nix. A numerical study of long range internal stresses associated with subgrain boundaries. *Acta Metall.*, 28 :1743–1752, 1980.

S. Haouala, S. Lucarini, J. Llorca, and J. Segurado. Simulation of the Hall-Petch effect in FCC polycrystals by means of strain gradient crystal plasticity and FFT homogenization. *J. Mech. Phys. Solids*, 134, 2020.

S. He, B. He, K. Zhu, and M. Huang. Evolution of dislocation density in bainitic steel : Modeling and experiments. *Acta Mater.*, 149 :46–56, 2018.

J. Hirth and J. Lothe. *Theory of Dislocations*. Krieger Publishing Company, 1982.

T. Hsieh and R. Balluffi. Observations of roughening/de-faceting phase transitions in grain boundaries. *Acta Metall.*, 37(8) :2133–2139, 1989.

S. Huang, M. Huang, and Z. Li. Effect of interfacial dislocation networks on the evolution of matrix dislocations in nickel-based superalloy. *Int. J. Plast.*, 110(June) :1–18, 2018.

J. Jiang, T. Britton, and A. Wilkinson. Evolution of dislocation density distributions in copper during tensile deformation. *Acta Mater.*, 61(19) :7227–7239, 2013.

M. Jiang, B. Devincre, and G. Monnet. Effects of the grain size and shape on the flow stress : A dislocation dynamics study. *Int. J. Plast.*, 113 :111–124, 2019.

S. Khan, H. Zbib, and D. Hughes. Modeling planar dislocation boundaries using multi-scale dislocation dynamics plasticity. *Int. J. Plast.*, 20 :1059–1092, 2004.

S. Kondo, T. Mitsuma, N. Shibata, and Y. Ikuhara. Direct observation of individual dislocation interaction processes with grain boundaries. *Sci. Adv.*, 2 (11) :e1501926, 2016.

E. Kröner. On the physical reality of torque stresses in continuum mechanics. *Int. J. Eng. Sci.*, 1(2) :261–278, 1963.

T. Lee, I. Robertson, and H. Birnbaum. TEM in situ deformation study of the interaction of lattice dislocations with grain boundaries in metals. *Philos. Mag. A*, 62(1) :131–153, jul 1990.

J. Li. Some elastic properties of an edge dislocation wall. *Acta Metall.*, 8(8) : 563–574, 1960.

J. Li and C. Needham. Some elastic properties of a screw dislocation wall. *J. Appl. Phys.*, 31(8) :1318–1330, 1960.

D. Liu and D. Dunstan. Material length scale of strain gradient plasticity : A physical interpretation. *Int. J. Plast.*, 98 :156–174, 2017.

V. Lubarda and D. Kouris. Stress fields due to dislocation walls in infinite and semi-infinite bodies. *Mech. Mater.*, 23(3) :169–189, 1996.

N. Malyar, G. Dehm, and C. Kirchlechner. Strain rate dependence of the slip transfer through a penetrable high angle grain boundary in copper. *Scripta Materialia*, 138 :88–91, 2017.

H. Mughrabi. Dislocation wall and cell structures and long-range internal stresses in deformed metal crystals. *Acta Metall.*, 31(9) :1367–1379, 1983.

H. Mughrabi. Dislocation clustering and long-range internal stresses in monotonically and cyclically deformed metal crystals. *Rev. Phys. Appl.*, 23(4) : 367–379, 1988.

T. Mura. *General theory of eigenstrains*. Springer Netherlands, Dordrecht, 1987.

J. Nye. Some geometrical relations in dislocated crystals. *Acta Metall.*, 1(2) : 153–162, 1953.

T. Ohashi, R. Barabash, J. Pang, G. Ice, and O. Barabash. X-ray microdiffraction and strain gradient crystal plasticity studies of geometrically necessary dislocations near a Ni bicrystal grain boundary. *Int. J. Plast.*, 25(5) :920–941, 2009.

W. Pantleon. Resolving the geometrically necessary dislocation content by conventional electron backscattering diffraction. *Scripta Materialia*, 58(11) : 994–997, 2008.

B. Peeters, B. Bacroix, C. Teodosiu, P. Van Houtte, and E. Aernoudt. Work-hardening/softening behaviour of b.c.c. polycrystals during changing strain paths : II. TEM observations of dislocation sheets in an IF steel during two-stage strain paths and their representation in terms of dislocation densities. *Acta Mater.*, 49(9) :1621–1632, 2001.

L. Priester. Grain Boundaries : From Theory to Engineering. In L. Priester, editor, *Grain Boundaries From Theory to Eng.* Springer Netherlands, Dordrecht, 2013.

C. Rey and G. Saada. The elastic field of periodic dislocation networks. *Philosophical Magazine*, 33(5) :825–841, 1976.

A. Roy and A. Acharya. Finite element approximation of field dislocation mechanics. *J. Mech. Phys. Solids*, 53(1) :143–170, 2005.

G. Saada and E. Bouchaud. Dislocation walls. *Acta Met. Mater.*, 41(7) :2173–2178, 1993.

K. Shih and J. Li. Energy of grain boundaries between cusp misorientations. *Surf. Sci.*, 50(1) :109–124, 1975.

F. Sun, E. Meade, and N. O'Dowd. Strain gradient crystal plasticity modelling of size effects in a hierarchical martensitic steel using the Voronoi tessellation method. *Int. J. Plast.*, 2019.

S. Sun, B. Adams, and W. King. Observations of lattice curvature near the interface of a deformed aluminium bicrystal. *Philosophical Magazine A*, 80 (1) :9–25, 2000.

A. Sutton and R. Balluffi. *Interfaces in Crystalline Materials*. Oxford University Press, 1995.

X. Wu, M. Yang, F. Yuan, G. Wu, Y. Wei, X. Huang, and Y. Zhu. Heterogeneous lamella structure unites ultrafine-grain strength with coarse-grain ductility. *Proc. Natl. Acad. Sci. U. S. A.*, 112, 2015.

Y. Yang, L. Wang, C. Zambaldi, P. Eisenlohr, R. Barabash, W. Liu, M. R. Stoudt, M. A. Crimp, and T. R. Bieler. Characterization and modeling of heterogeneous deformation in commercial purity titanium. *Jom*, 63(9) :66–73, 2011.